Journal of Materials Chemistry A

The roles of oxygen vacancies, electrolyte composition, lattice structure, and doping density on the electrochemical reactivity of Magnéli phase TiO_2 anodes

Journal:	*Journal of Materials Chemistry A*
Manuscript ID	TA-ART-04-2018-003719.R1
Article Type:	Paper
Date Submitted by the Author:	23-Oct-2018
Complete List of Authors:	Jing, Yin; University of Illinois at Chicago, Chemical Engineering Almassi, Soroush; University of Illinois at Chicago, Chemical Engineering Mehraeen, Shafigh; University of Illinois at Chicago, Chemical Engineering LeSuer, Robert; SUNY Brockport Chaplin, Brian; University of Illinois at Chicago, Chemical Engineering

The roles of oxygen vacancies, electrolyte composition, lattice structure, and doping density on the electrochemical reactivity of Magnéli phase TiO_2 anodes

Yin Jing,[a] Soroush Almassi,[a] Shafigh Mehraeen,[a] Robert J. LeSuer,[b] Brian P. Chaplin[a*]

[a] *Department of Chemical Engineering, University of Illinois at Chicago, 810 South Clinton Street, Chicago, Illinois 60607, United States*

[b] *Department of Chemistry, The College at Brockport, State University of New York, Brockport, New York 14420, United States*

* *Corresponding author. Phone: (+1)312-996-0288; Fax: (+1)312-996-0808; E-mail: chaplin@uic.edu.*

† Electronic Supplementary Information (ESI) available: extra experimental and simulation details and results

Abstract

Substoichiometric TiO_2 (Ti_nO_{2n-1}, $4 \leq n \leq 10$) is a promising and cost-effective material, that is being investigated for many applications, such as information storage, energy storage and conversion, and water treatment. Upon extended anodic polarization, Ti_nO_{2n-1} reportedly suffers from gradual loss in conductivity and electrochemical reactivity. In this study, the surface deactivation and reactivation mechanisms were examined on a Ti_nO_{2n-1} monolithic electrode in three different electrolyte solutions (i.e., H_2SO_4, $HClO_4$, HCl). The intrinsic electronic properties, charge transfer kinetics, crystalline structure, and surface composition were examined experimentally after anodic and cathodic polarizations. Statistically equivalent results were obtained from local scanning electrochemical microscopy (SECM) and bulk electrochemical impedance spectroscopy measurement, which indicate that spatially resolved SECM data accurately characterized charge transfer kinetics of the Ti_nO_{2n-1} electrode at the micron-scale. Results indicate that decreases in conductivity and charge transfer kinetics after anodic polarizations in all three electrolytes were primarily attributed to the loss of charge carriers, such as H^+ discharge at Ti^{3+} point donor sites, and the process was reversible during cathodic polarization via H^+ intercalation. In the H_2SO_4 electrolyte reversible surface passivation also occurred, which was attributed to the formation of $TiOSO_4$ surface species whose presence were supported by experimental measurements and density functional theory calculations. It was also determined that the Ti_nO_{2n-1} crystal structure directly affected the hydroxyl radical formation rate, with the highest rate observed for Ti_4O_7, which also possessed the highest charge carrier density.

Keywords: substoichiometric TiO_2, surface deactivation and reactivation, scanning electrochemical microscopy, intercalation

1. Introduction

The creation of oxygen vacancies, which act as electron donor sites, is an important method that can be used to modify the electronic and optical properties of most transition metal oxide based semiconductors.[1–3] Among these metal oxides, TiO_2 generally exhibits high environmental compatibility, chemical stability, and low cost.[4] The synthesis of substoichiometric TiO_2 is one approach being actively researched to overcome its wide band gap (E_g = 3.0 eV).[2,5,6] Substoichiometric TiO_2 is synthesized by creating oxygen vacancies in the lattice structure of TiO_2, resulting in rearrangement of the crystal structure. The changes in the crystal structure are accompanied by changes in the electronic, charge transport, and surface chemical properties.[7,8] Depending on the extent of oxygen deficiencies, a series of substoichiometric TiO_2 phases, or Magnéli phases, with a general formula of Ti_nO_{2n-1} ($4 \leq n \leq 10$) can be obtained. The structure of Ti_nO_{2n-1} can be described as consisting of rutile-like chains (edge- and corner-sharing arrangement) of n TiO_6 octahedra units along the c-direction bounded by a corundum layer (Ti_2O_3). Therefore, from this point of view, Magnéli phases can be interpreted as an ordered combination of rutile TiO_2 and corundum Ti_2O_3 layers, and the Ti_2O_3 boundaries are usually referred to as the shear planes. The oxidation state of Ti atoms is altered as a result of these oxygen vacancies. The Ti atoms in defect-free TiO_2 are in the 4+ oxidation state. The removal of a bridging oxygen atom, which is more energetically favorable compared to in-plane oxygen atom removal, leaves two subsurface Ti^{3+} sites exposed.[9] The average electronic charge of a specific Magnéli phase is determined by the ratio of Ti^{3+} to Ti^{4+}, that forms a shear structure by electron sharing.[10] Among the Magnéli phases, Ti_4O_7 ($Ti^{3.5+}$) consists of an equal proportion of Ti^{3+} and Ti^{4+} atoms, where the d-band electrons are fully delocalized and therefore possesses the highest electrical conductivity.[11] The Magnéli phases can undergo metal-insulator transition under the control of

external stimuli, such as temperature, light, and pressure, and thus can be readily used as memristive material for memory and switching devices, or thermoelectric material in electric power generation.[12–15] The superior electronic properties also make Magnéli phases an ideal material for electrodes in electrochemical advanced oxidation processes (EAOPs),[16–21] visible light photocatalysis,[22,23] and energy storage[4,24–28] and conversion.[29–32]

Despite the great potential of the Ti_nO_{2n-1} material discussed above, it is reported that Ti_nO_{2n-1} suffers from a gradual loss of conductivity during anodic polarization, especially when polarized in a sulfate electrolyte.[7,20,24,33] The sulfate ion is used as an electrolyte in lead acid and vanadium redox flow batteries and is abundant in various wastewater solutions.[7,20,24,33,34] While a change in conductivity is key to the operation of memristive devices, it leads to capacity loss from ohmic drop and less stable cycling in energy storage and conversion devices,[35] and a decrease in hydroxyl radical ($OH^{\bullet}$) production during EAOPs and photocatalytic processes.[36] Several authors have studied the gradual loss of electrode activity by studying the physical, chemical, and electrical properties through monitoring X-ray diffraction (XRD),[24] X-ray photoelectron spectroscopy (XPS),[37] and electrochemical impedance spectroscopy (EIS) measurements,[7] as well as the oxidation kinetics of model compound removal.[20,33] However, the mechanisms of surface deactivation are still unclear. Chen *et al.* proposed the loss of Ti_nO_{2n-1} activity in a 0.5 M H_2SO_4 electrolyte was due to the irreversible conversion of Ti^{3+} to Ti^{4+} after a 7-hour anodic polarization at 7 mA cm^{-2}.[7] In the same electrolyte, the phase change from Ti_4O_7 to Ti_6O_{11}, as supported by XRD, was observed by Kao *et al.*, when the electrode was cycled between 1.7 V and 2.6 V vs Ag/AgCl.[24]

All previous studies that focused on variations of conductivity and electrochemical reactivity of Ti_nO_{2n-1} utilized bulk electrochemical characterization techniques to elucidate the

overall change in the interfacial charge transfer properties, which represent an average for the entire surface. To resolve the surface heterogeneity and local reactivity, studies employed scanning electrochemical microscopy (SECM) to provide spatial resolution of intrinsic charge transfer kinetics at the electrode/electrolyte interface.[38–41] The kinetic heterogeneity originates from the tunneling rate of electrons/holes to the redox active species in solution, and therefore slow kinetics occur when either the charge carriers are deep inside the material and slow to migrate to the surface, or charge carrier density (N_D) is low.[40] The operation of SECM is based on the measurement of the current through a redox reaction at an ultramicroelectrode (UME) tip with a radius on the order of tens of nanometers to tens of microns, when it is positioned near a substrate electrode surface.[42] The perturbation in current response of the UME tip in the presence of the substrate electrode provides information about the conductivity, electron transfer reaction kinetics, and topography of the substrate with tip size resolution.

The focus of this work was on determining mechanisms for anodic passivation and cathodic reactivation of a Ti_4O_7 anode. The anodic stability of Ti_4O_7 was assessed in three supporting electrolytes (HCl, $HClO_4$, and H_2SO_4), and the effect of different Magnéli phases on the $OH^{\bullet}$ production rates was examined. A methodology was developed to study changes in charge-transfer kinetics at specific locations on a Ti_nO_{2n-1} electrode as a function of anodic and cathodic applied charges. The crystalline structure was monitored by XRD, and the variations in the electronic conductivity were evaluated by Mott-Schottky analysis and film resistivity (ρ_f) measurements. The changes of local and bulk charge transfer kinetics were investigated using SECM and EIS, respectively. Findings from this work provided a greater understanding of the anodic stability of Ti_nO_{2n-1}, that is an important factor for the successful operation of water treatment and energy

storage and conversion technologies, and also offer insights for improving material manufacture and operational strategies.

2. Experimental

2.1 Reagents. Titanium(IV) oxide, hexaammineruthenium(III) chloride ($Ru^{[III]}Hex$), potassium dihydrogen phosphate, potassium chloride, paraffin oil, sulfuric acid, hydrochloric acid, perchloric acid, and terephthalic acid were reagent-grade and obtained from Sigma-Aldrich (St. Louis, MO) and used as received. All solutions used in this study were made with deionized (DI) water obtained from a NANOPure water purification system (Barnstead Nanopure, Thermo Scientific, Waltham, MA) with resistivity greater than 18.2 MΩ cm (25° C).

2.2 Preparation of Ti_nO_{2n-1} electrode. Anatase TiO_2 powder was reduced to Ti_nO_{2n-1} in a tube furnace (OTF-1200X, MTI) at a temperature of 1050 °C and 1.0 atm flowing H_2 for 6 hours. The monolithic electrode was prepared by mixing 0.78 g of Ti_nO_{2n-1} powder with 0.12 g of paraffin oil as binder, and the mixture was then pressed into a pellet form using an industrial hydraulic press (RAMCO, Kent, WA) under a 17.2 bar uniaxial pressure in a 1.12 cm diameter die, which produced a pellet thickness of ~3.4 mm. The paraffin oil binder was removed in the furnace at a temperature of 1050 °C in 1.0 atm flowing Ar for 6 hours to produce a binder-free Ti_nO_{2n-1} porous pellet.

The binder-free Ti_nO_{2n-1} pellet was then mounted in a rotating disk electrode holder and attached to a rotator (Pine Research Instruments; MSR rotator; Durham, NC), and polished with grade 800 sandpaper (3M, St. Paul, AK), followed by alumina/DI water slurries (alumina particle diameters: 1.0, 0.3 and 0.05 μm) under a rotation speed of 900 rotations per minute (rpm) for 5, 10, and 15 mins with each particle size. The Ti_nO_{2n-1} pellet was sonicated in DI water in a sonicator

(Model: 08895-38, Cole-Parmer) for 5 min, and then rinsed with ethanol to remove residual particles, followed by DI water to remove the residual ethanol.

2.3 Electrode Markers. In order to characterize charge-transfer kinetics at specific locations during repeated SECM measurements, electrode positioning markers were etched on the Ti_nO_{2n-1} electrode using a TYKMA Electrox laser marking system (EMS300, Chillcothe, OH) with 30% laser power (1.36 kW absolute power) and 200 mm s^{-1} traveling speed (repeated 15 times). These markers allowed for a triangulation method to be used to resample the same spots on the electrode. A pattern containing three positioning markers, as shown in the ESI (Figure S-1), was created on the electrode using the laser marking system. Details of laser marking and pattern examination are provided in the ESI (Section S-1).

2.4 Electrochemical Methods.

2.4.1 SECM Experiments. SECM experiments were performed with a CH Instruments model 920d scanning stage and bipotentiostat (CH Instruments, Austin, Texas). The Ti_nO_{2n-1} electrode was mounted at the bottom of a Teflon electrochemical cell. SECM measurements were performed using a four-electrode setup. A Pt UME (CHI116, CH Instruments) with 10 μm diameter and the Ti_nO_{2n-1} electrode were both working electrodes. A shared 0.3 mm diameter Pt wire was used as the counter electrode and saturated Ag/AgCl as the reference electrode. The ratio of glass radius to disk radius (*RG*) for the Pt UME was determined as 2.98, by fitting the negative feedback equation developed by Lefrou and Cornut[43] to the probe approach curve data for a UME approaching a glass substrate at -0.3 V vs Ag/AgCl tip potential in a 5 mM $Ru^{[III]}$Hex and 100 mM KCl electrolyte. The value for *RG* was recorded after each polishing with 0.05-micron alumina powders and substantial variations were not observed (*RG* = 2.97-3.01). In our experiments, tip velocities of 4 μm s^{-1} and 1 μm s^{-1} were used for stepper motor and piezo nanopositioner

movements, respectively. The local kinetic measurements were obtained in a solution of 5 mM $Ru^{[III]}$Hex and 100 mM KCl, with a constant tip potential of -0.3 V vs Ag/AgCl to reach the steady state current for $Ru^{[III]}$Hex reduction to $Ru^{[II]}$ in the feedback mode (See ESI Figure S-2), while the substrate potential was held at 0 V vs Ag/AgCl. All SECM measurements were made at room temperature (22 °C ± 1 °C).

2.4.2 EIS and Mott-Schottky Analyses. The potentiostatic EIS and Mott-Schottky analyses were performed with a Gamry potentiostat (Interface 1000, Warminster, PA) and used a three-electrode setup with the Ti_nO_{2n-1} electrode as working electrode, 0.5 mm diameter Pt wire as counter electrode, and saturated Ag/AgCl as reference electrode. EIS measurements were made at the open circuit potential (OCP, 0.03 V vs Ag/AgCl) in an electrolyte containing 5 mM $Ru^{[III]}$Hex and 100 mM KCl, with an amplitude of 4 mV in the sinusoid perturbation, and over a frequency range of 30 kHz to 100 mHz. Mott-Schottky measurements were recorded at ±1 V of the OCP, at a frequency of 30 kHz, a voltage step of 0.05 V, and an amplitude of 4 mV perturbation in a 100 mM $NaClO_4$ electrolyte. A constant temperature was maintained in both measurements at 25 °C using a glass, jacketed reactor and a recirculating water bath (Thermo Scientific, Neslab RTE 7).

2.4.3 Anodic Ageing and Cathodic Reactivation Experiments. Anodic ageing and cathodic reactivation were performed in 1 M H_2SO_4, 2 M $HClO_4$, and 2 M HCl electrolytes for 30 minutes at applied current densities of 20 mA cm^{-2} and -20 mA cm^{-2}, respectively, and at a constant temperature of 25 °C. The corresponding averaged anodic potentials, corrected for solution resistance, in H_2SO_4, $HClO_4$, and HCl were 2.8 ± 0.5, 2.7 ± 0.4, and 2.6 ± 0.3 V vs Ag/AgCl, respectively. The corresponding averaged cathodic potentials, corrected for solution resistance, in H_2SO_4, $HClO_4$, and HCl were -0.7 ± 0.1, -0.8 ± 0.2, and -0.8 ± 0.1 V vs Ag/AgCl, respectively. Control experiments were performed in the same electrolyte solutions at the OCP for 30 minutes.

2.4.4 Topographic Mapping. The topography on a specific area of the Ti_nO_{2n-1} electrode was determined by measuring the O_2 reduction current at the UME tip at an applied potential of -0.4 V vs Ag/AgCl in a 100 mM $NaClO_4$ electrolyte, while Ti_nO_{2n-1} was left at the OCP (~ 0.1 V vs Ag/AgCl). The justification of this method was detailed in the ESI (Section S-3). The amperometric mapping of the O_2 reduction current over a specific area was converted to a topographic map by using the equations developed by Lefrou and Cornut.[43] Briefly, the negative feedback equation described the relationship between the tip current and the tip-to-substrate distance, and a Matlab script was used to solve the relative distance by taking the current at each point from the amperometric map.

The surface roughness (S_a) can be calculated from the topographic mapping by using Equation 1.

$$S_a = \frac{1}{A}\int_0^{L_y}\int_0^{L_x} |Z(x,y)|dxdy \tag{1}$$

where A (μm^2) is the projected surface area, $|Z(x, y)|$ is the absolute value of profile height over a given area ($dxdy$), L_y (μm) and L_x (μm) are the length and width, respectively.

2.4.5 Kinetic Rate Constant Mapping. In order to obtain a spatial kinetic rate constant map of the Ti_nO_{2n-1} surface, the SECM data were processed using the method developed by Mirkin *et al*.[44] Briefly, the normalized kinetic controlled current (Ni_s) was obtained by solving Equation 2.

$$Ni_{tot} = Ni_s\left(1 - \frac{Ni_T^{ins}}{Ni_T^{cond}}\right) + Ni_T^{ins} \tag{2}$$

where Ni_{tot} is the normalized current obtained for $Ru^{[III]}Hex$ reduction at the UME, Ni_T^{ins} is the normalized current obtained for O_2 reduction, and Ni_T^{cond} is the normalized current over a conductor, which can be calculated using Equation 3.

$$Ni_T^{cond} = \frac{0.78377}{L} + 0.3315 \times \exp\left(-\frac{1.0672}{L}\right) + 0.68 \tag{3}$$

where L is the normalized distance defined as the ratio of the tip-to-substrate distance and the UME radius, which was calculated as described in Section 2.4.4. Therefore, the normalized kinetic rate constants (Λ) were determined by solving Equation 4 at each data point (1.0 μm x-y discretization).

$$Ni_s = \frac{0.78377}{L + \frac{1}{\Lambda}} + \frac{0.3315 \times \exp\left(-\frac{1.0672}{L}\right) + 0.68}{1 + \left[\frac{\frac{11}{\Lambda L} + 7.3}{110 - 40L}\right]} \tag{4}$$

2.5 Thermogravimetric Analysis (TGA). TGA measurements were performed using a Mettler thermogravimetric analyzer (TGA 2, Leicester, UK) under flowing air. Sample weight was normalized to the initial weight. In order to calculate the activation energy required to convert Ti_4O_7 to a given higher oxidation state phase, four ramp rates of 5, 10, 20, and 40 °C min^{-1} were chosen, and the equation used for calculating the activation energy (E_a) is given by Equation 5.

$$E_a = -R\frac{dln\beta}{d\frac{1}{T}} \tag{5}$$

where β (°C min^{-1}) is the heating rate, T (°K) is the temperature at which the weight ratio in the TGA plot matches with the molecular weight ratio of a given Magnéli phase to that of Ti_4O_7, and R (8.314 J K^{-1} mol^{-1}) is the gas constant.

2.6 Kinetic Analysis of Different Magnéli Phases for OH• Production. Porous Ti_nO_{2n-1} samples of different Magnéli phases were prepared as follows. First, 5 pristine samples were prepared as described in Section 2.2. Samples 2 to 5 were heated in air from room temperature to 466, 484, 495, and 501 °C at a heating ramp of 5 °C min^{-1} and the resulting weight gain was monitored by TGA analysis (ESI Figure S-18). These samples were expected to be Ti_5O_9, Ti_6O_{11}, Ti_7O_{13}, and Ti_8O_{15}, while Sample 1 was left untreated. The actual phases of these samples were determined by XRD, and an average value of n in each converted sample was estimated using Equation 6.

$$\frac{M_{TiO_{\frac{2n-1}{n}}}}{M_{TiO_{\frac{7}{4}}}} = \frac{48 + 16 \times \frac{2n-1}{n}}{48 + 16 \times \frac{7}{4}} = \frac{m_{TiO_{\frac{2n-1}{n}}}}{m} \quad (6)$$

where $M_{\mathrm{TiO}_{\frac{2n-1}{n}}}$ and $M_{\mathrm{TiO}_{\frac{7}{4}}}$ (g mol^{-1}) are the molecular weights of the converted sample (Ti_nO_{2n-1}) and pristine sample (Ti_4O_7), respectively. Meanwhile, $m_{\mathrm{TiO}_{\frac{2n-1}{n}}}$ and m (g) are the measured masses of the converted and pristine samples, respectively.

In order to examine the OH• production rate on the different electrode samples, a dead-end flow-through reactor setup was used (Figure 1). A solution containing 0.1 mM terephthalic acid in 1 M KH_2PO_4 (pH = 4.5) supporting electrolyte was pumped through the porous Ti_nO_{2n-1} samples polarized at an anodic potential of 3.5 V vs Ag/AgCl. Terephthalic acid is a well-accepted OH• probe that produces 2-hydroxyterephthalic acid, and the analytical method used for terephthalic acid and 2-hydroxyterephthalic acid quantification was described previously.[45] The solution resistance, measured by EIS, ranged between 11.6 and 17.2 ohm for experiments performed on Samples 1-5, resulting in solution resistance corrected anodic potentials of 3.3 ± 0.1 V vs. Ag/AgCl.

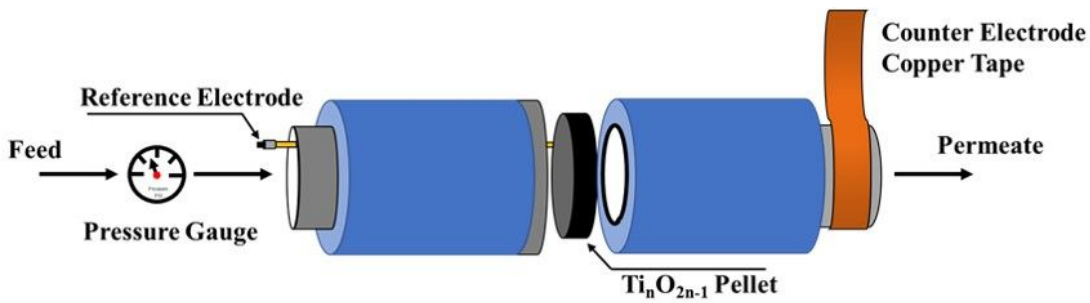

Figure 1 Schematic of the dead-end flow-through reactor setup for the assessment of $OH^{\bullet}$ production on Ti_nO_{2n-1} electrodes.

The lower bound estimates of the surface concentration of $OH^{\bullet}$ at steady state ($[OH^{\bullet}]_s$) was calculated using Equation 7.[46]

$$[OH^{\bullet}]_s = \frac{k_{TA}}{k_{TA,OH^{\bullet}}} \quad (7)$$

where $k_{TA,OH^{\bullet}}$ = 4.0 x 10^6 m^3 $mole^{-1}$ s^{-1},[47] and k_{TA} (m s^{-1}) is the first-order nominal surface area normalized observed rate constant for terephthalic acid oxidation determined from the experiment.

2.7 Quantum Mechanical Calculations. Density functional theory (DFT) simulations were performed to determine the adsorption energy (ΔU_a) for the adsorption of sulfate species to titanium suboxide. The DFT calculations were performed on a Ti_4O_7 (1-20) periodic slab model. The calculation of Gibbs free energy of activation (E_a) vs. electrode potential for the oxidation of SO_4^{2-} by an outer electron transfer reaction was determined according to Marcus theory.[45,48] DFT calculations of sulfate oxidation were performed using the Gaussian 16 software.[49] Unrestricted spin, all-electron calculations were performed using the 6-31G++(d) basis set for geometry optimization and energy calculations. The gradient corrected Becke, three-parameter, Lee−Yang−Parr (B3LYP) functional was used for exchange and correlation. Implicit water solvation was incorporated using the SMD model.[50]

In the periodic slab model, the first-principle calculations were performed using the projector augmented wave (PAW) within the Vienna *ab initio* Simulation Package (VASP) based on DFT.[51–54] Nonlocal exchange correlation energy was evaluated using the Perdew-Burke-Emzehof (PBE) functional. The electron wave function was expanded using plane waves with a cut-off energy of 570 eV. All structures were optimized with force convergence of 10 meV $Å^{-1}$. The optimized bulk unit cell of Ti_4O_7 was cleaved on the (1-20) plane and the surface was modeled using a (2 × 2 × 1) super cell consisting of 32 Ti and 60 O atoms distributed in four layers, in which the vacuum layer is set to 15.0 Å. The uppermost surface layer and the sulfate molecule were allowed to relax. An 8 × 8 × 1 Monkhorst-Pack *k*-point mesh was automatically generated for the Brillouin zone sampling for the super cell. A neutral charge was assumed for the simulation of the complexed system, as excessive electrons from either sulfate anion or radical were considered to be delocalized on a conductive substrate. For sulfate anion and radical, the number of electrons were set using NELECT in the VASP. The value of ΔU_a was defined as the difference between the total electronic energies of the adsorbed system and the isolated adsorbate and the Ti_4O_7 slab at a given electrode potential. Image structures were created using VESTA 3.0 software.[55]

3. Results and Discussion

3.1 Examination of Crystalline Structure and Electronic Properties during Electrolysis. In each of the three supporting electrolytes, a pristine Ti_nO_{2n-1} sample was first subjected to anodic ageing for 30 minutes, and then followed by the cathodic reactivation for a given time. Figure 2 shows the XRD patterns of Ti_nO_{2n-1} samples under these three different states. The estimated crystal sizes of the pristine samples by the Scherrer equation, in Figure 2A – 2C, are 92 ± 10, 79 ± 4 and 103 ± 22 nm, and similar crystal sizes are estimated after anodic ageing and cathodic reactivation for all Ti_nO_{2n-1} samples (ESI Table S-1 to S-3). In analyzing XRD

patterns, the 2θ angle at 20.78° is used as the characteristic peak for Ti_4O_7 identification. Pristine Ti_nO_{2n-1} samples, as shown in Figure 2A-2C, all consist of high purity Ti_4O_7, the pattern matches the Joint Committee on Powder Diffraction Standards (JCPDS) card no. 00-050-0787 without any detectable crystalline impurities. The XRD pattern changes relative to the pristine state after the anodic ageing in the H_2SO_4 electrolyte, where new dominant peaks at 13.84° and 22.80° are observed. Observable changes to the XRD patterns are not identified for samples polarized in the $HClO_4$ and HCl electrolytes. The appearance of the peaks at 13.84°, 22.80°, 26.63°, and 27.61° strongly suggest the formation of a $TiOSO_4$ film, since all *2θ* positions are representative of the $TiOSO_4$ crystal structure (JCPDS no. 01-085-2452). The corresponding crystal facets of these *2θ* angles are labeled in Figure 2A, and the crystal size of the sample in Figure 2A is estimated as 100 ± 11 nm, which is statistically identical to Ti_nO_{2n-1} samples (ESI Table S-4). Figure 2D shows the characteristic peaks of Ti_4O_7 slightly shift to higher and back to low *2θ* angles upon anodic ageing and cathodic reactivation in $HClO_4$ electrolyte, respectively, which is also observed in the other two electrolytes (Figure 2A and 2C). The shift in the characteristic peaks is likely caused by the distortion of the crystal framework, which suggests the release and intercalation of small guest ions in the lattice structure, considering that crystal size and lattice strain do not change significantly (ESI Table S1-S4).[56–58] The peak area ratio (*PR*) of the peak at 22.80° to the characteristic peak of Ti_4O_7 is used to quantify the variation in crystalline structure in the H_2SO_4 electrolyte, and is calculated as 0.10 at the pristine state, when the background intensity (signal noise) at 22.80° position is used for calculation, since a peak is not found at this position. The value for *PR* increases to 1.02 after the anodic ageing, decreases to 0.51 and 0.11 after the 1st 30-min and 2nd 120-min cathodic reactivations, respectively (Figure 2A). The value for *PR* after the 2nd 120-min cathodic reactivation is almost identical to that at the pristine state, and it demonstrates

the crystal structure of the electrode is restored to its original state. Meanwhile, the disappearance of both peak at 13.84° and 22.80° indicates the removal of the $TiOSO_4$ film from the electrode to levels less than the detection limit.

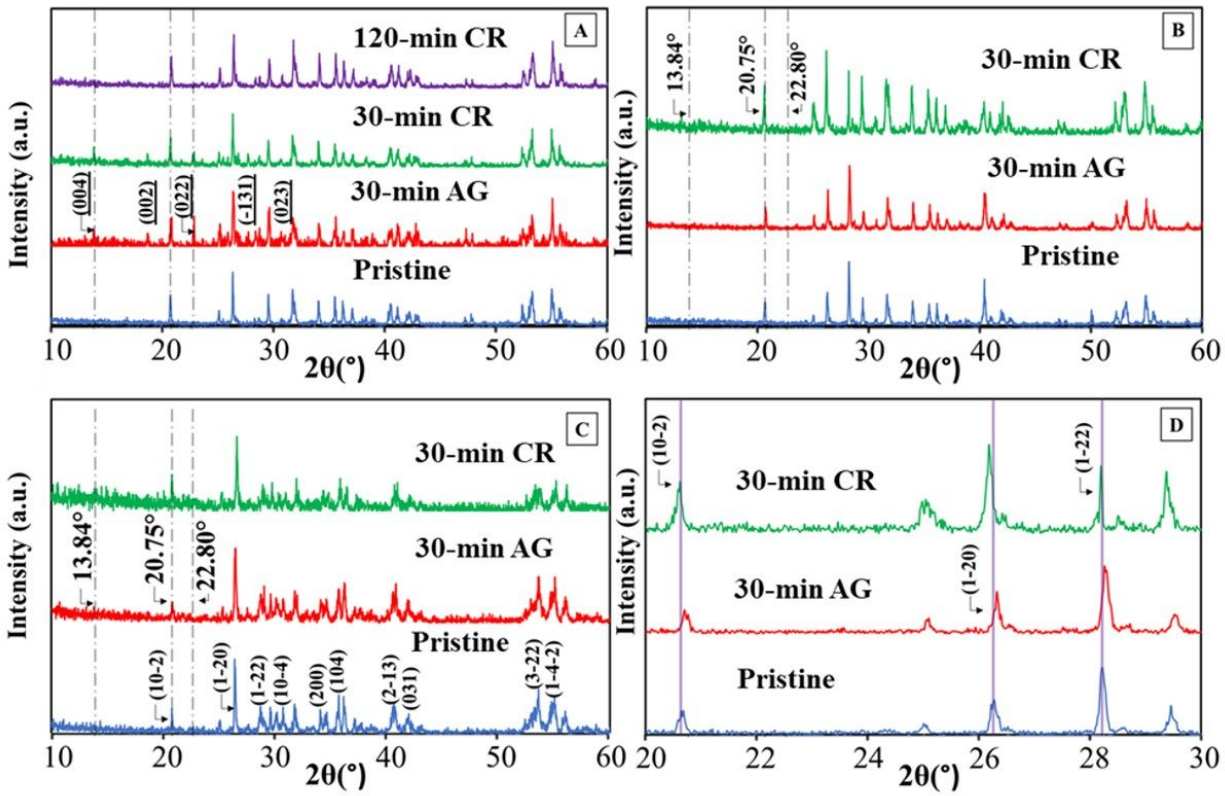

Figure 2 XRD patterns of the Ti_nO_{2n-1} samples at pristine state and after anodic ageing and cathodic reactivations in (A) 1 M H_2SO_4, (B) 2 M $HClO_4$, and (C) 2 M HCl solutions. (D) Details of the XRD patterns between 2θ angles of 20° and 30° (data from Figure 2B). Characteristic peaks at 13.84° ($TiOSO_4$), 20.78° (Ti_4O_7), and 22.80° ($TiOSO_4$ and/or Ti_6O_{11}) are shown as the vertical dashed lines. AG and CR stand for anodic ageing and cathodic reactivation, respectively.

Mott-Schottky plots indicate that the Ti_4O_7 electrode is an *n*-type semiconductor, as confirmed by the positive slope, which is consistent with prior studies (ESI Figure S-4).[59] Characterization of N_D , flat band potential (E_{fb}), and ρ_f (ESI Table S-5) are also used to examine changes to the electronic properties as a result of the electrochemical treatments. The results are similar in all three electrolytes. The values for N_D decrease upon anodic ageing and increase after

cathodic reactivation, while an opposite trend is observed for ρ_f and E_{fb}. As shown in the ESI (Table S-5), the values for N_D decrease to 2.2, 6.6, and 27% of the pristine states after the anodic ageing, and increase to 30, 26, and 55% of the pristine states after the 30-min cathodic reactivation in H_2SO_4, $HClO_4$, and HCl electrolytes, respectively. The value for N_D increases to 52% of the pristine state after the 2nd cathodic reactivation in H_2SO_4. The values for E_{fb} vary from -0.59 ± 0.02 to -0.84 ± 0.02 V vs Ag/AgCl (ESI Table S-5), which are comparable to those measured on a N-doped TiO_2 film (-0.75 to -0.65 V vs Ag/AgCl).[5] The value of E_{fb} shifts to more negative potentials after the anodic ageing, and does not vary noticeably after the cathodic reactivation. This observation suggests that the depletion layer thickness of a pristine Ti_nO_{2n-1} is smaller than that after the anodic ageing or cathodic reactivation, which results in a faster charge transfer rate at the pristine electrode.[60] Values for ρ_f, relative to the pristine state, increase to 711, 632, and 647% after the anodic ageing, and decrease to 182, 130, and 115% after the 30-min cathodic reactivation in H_2SO_4, $HClO_4$ and HCl electrolytes, respectively. The value for ρ_f further decreases to 129% of the pristine state after the 2nd cathodic reactivation in H_2SO_4. The changes in ρ_f are likely attributed to the changes in the shallow dopant concentration.

The XRD results indicate that a crystal structure change is only associated with anodic ageing of Ti_nO_{2n-1} in the H_2SO_4 electrolyte, which is reversible upon cathodic reactivation. These changes are attributed to electrochemical polarizations, since changes in the XRD spectra are not observed when the sample is left at the OCP in the H_2SO_4 electrolyte (ESI Figure S-6). Furthermore, identification of peaks associated with $TiOSO_4$ suggests that SO_4^{2-} or its radical form ($SO_4^{\bullet-}$), *via* the oxidation of SO_4^{2-}, interacts with surface Ti sites more strongly than Cl^- and ClO_4^- upon anodic ageing, which will be discussed in more detail in Section 3.4. Although crystal structure changes are not observed in either $HClO_4$ or HCl electrolytes, variations in N_D and ρ_f are

still observed during anodic ageing and cathodic reactivation. These changes are unlikely due solely to $Cl^{\bullet}$ produced *via* the oxidation of Cl^{-}, since changes in N_D and ρ_f are also observed after the electrolysis of $HClO_4$, which is an inert electrolyte. These changes are possibly attributed to a variation in dopant concentration that is caused by the oxidation of Ti^{3+} sites and the discharge of protons during anodic ageing, as well as the reduction of Ti^{4+} and the intercalation of protons during cathodic reactivation.[46,61–63] This mechanism is also suggested as the primary factor for the increase in conductivity during the synthesis of reduced TiO_2 nanotubes via electrochemical reduction in an aqueous electrolyte.[46]

3.2 Variation in Local and Bulk Charge Transfer Kinetics During Electrolysis. As discussed above, the changes in the electronic properties (i.e., N_D and ρ_f) occur during anodic ageing and cathodic reactivation, and in turn would also affect the charge transfer kinetics of Ti_nO_{2n-1} at the electrode/electrolyte interface. To obtain a better understanding of the effect substrate polarization had on interfacial charge transfer, the local and bulk charge transfer kinetics were examined using SECM and EIS, respectively. Herein, the observed rate constant will be presented as a percent value relative to the rate constant observed at a pristine substrate. In the SECM characterization, 80 × 80 μm^2 surface images were analyzed on five well-separated areas (i.e., > 300 μm apart), and four approach curves were collected in each area to resolve the local charge transfer kinetics. While discussing the local kinetics, only one set of surface images at pristine, post anodic ageing, and after the 1st 30-min cathodic reactivation conditions in 1 M H_2SO_4 electrolyte are discussed as a representative data set, the other images and kinetic data are summarized in the ESI (Section S-10 to S-13).

The local and bulk charge transfer kinetics were studied using the redox reaction of the $Ru^{[II]}$Hex and $Ru^{[III]}$Hex redox couple at the working electrode, due to facile outer sphere electron

transfer kinetics and the lack of electrode fouling with this redox couple at either the Pt UME or substrate surfaces.[38] Figure 3A shows the pure topographic information of this specific area obtained by O_2 reduction, while Figures 3B to 3D show the surface images of mixed kinetics and topography of the pristine sample, after anodic ageing, and after the 30-min cathodic reactivation, respectively. The value for S_a is calculated as 2.1 ± 0.5 μm from 5 topographic images, which is comparable to the surface profilometer measurement (2.4 ± 0.3 μm), and confirms the robustness of the SECM method for topographic mapping. The topographic images remain almost identical among experiments (ESI Figure S-13), which suggests the differences in currents observed for $Ru^{[III]}$Hex reduction at the UME (Figure 3B to 3D) are dominated by changes in charge transfer kinetics at the substrate. The averaged normalized currents over the images are calculated as 1.26 ± 0.04 for the pristine sample, 1.08 ± 0.01 after anodic ageing, and 1.20 ± 0.02 after the 30-min cathodic reactivation. The trend in current indicates a decrease in electrochemical reactivity after anodic ageing, and partial recovery after the 1st 30-min cathodic reactivation, which agrees with the measurements for N_D and ρ_f. The approach curve method is used to measure the normalized current at four distinct spots shown as dashed circles in Figure 3B to 3D, and the normalized rate constants are determined by fitting the equation developed by Lefrou and Cornut for a kinetic controlled system to the data (see details in ESI Section S-13).[43] Compared to the pristine state, the rate constants at the post anodic ageing and 30-min cathodic reactivation are 65 ± 6% and 85 ± 4% in the H_2SO_4 electrolyte, 87 ± 5% and 93 ± 2% in the $HClO_4$ electrolyte, and 89 ± 5% and 94 ± 2% in the HCl electrolyte, respectively (ESI Table S-6 to S-8). Results of the approach curve method indicate that the rate constants for $Ru^{[II]}$Hex oxidation is affected by the polarization treatments at the substrate. The variation in values determined for the rate constants upon anodic ageing and cathodic reactivation are likely due to the electrolyte type, as the greatest changes (65%

after the anodic ageing and 85% after the cathodic reactivation) in rate constant values are found in the H_2SO_4 electrolyte, while changes are comparable and insignificant in both $HClO_4$ and HCl electrolytes.

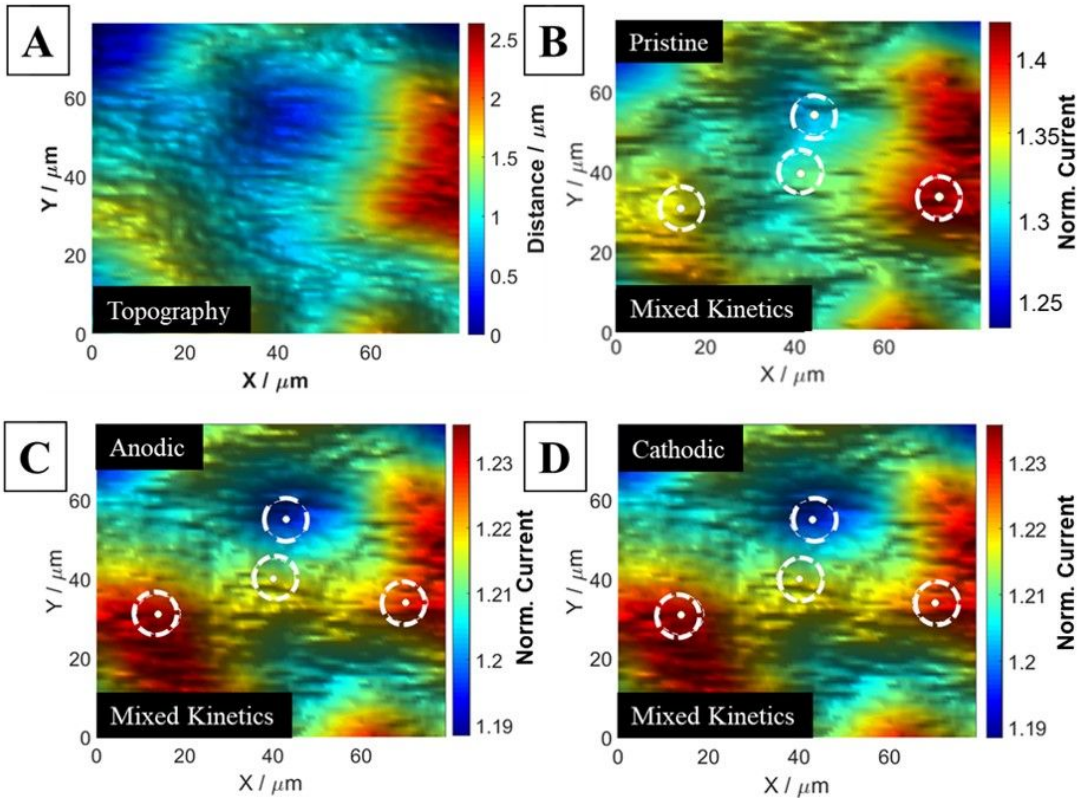

Figure 3 SECM images collected on the same area in the feedback mode. (A) Topographic mapping, amperometric mapping at (B) pristine, (C) post anodic ageing in H_2SO_4 electrolyte, and (D) post cathodic reactivation states in H_2SO_4 electrolyte. (Dashed circles represent the actual size of UME tip.)

Table 1 Normalized kinetic rate constant values estimated by three different methods. Values are normalized by the pristine sample and are reported in percent. Experiments in 1 M H_2SO_4, 2 M $HClO_4$, and 2 M HCl electrolyte after anodic ageing and cathodic reactivation. Errors represent standard deviations.

	Anodic Ageing			**Cathodic Reactivation**		
Electrolyte	**Bulk EIS**	**Approach Curve**	**Kinetic Mapping**	**Bulk EIS**	**Approach Curve**	**Kinetic Mapping**
H_2SO_4	34 ± 2	65 ± 6	41 ± 3	69 ± 4	85 ± 4	72 ± 4
$HClO_4$	49 ± 1	87 ± 5	68 ± 5	76 ± 3	93 ± 2	85 ± 4
HCl	50 ± 1	89 ± 5	69 ± 3	85 ± 1	94 ± 2	87 ± 4

Table 1 summarizes rate constants obtained from the bulk EIS measurements ($N_{\text{frequency}}$ = 56), local approach curves (N = 20), and local kinetic mapping (N = 32000). Results for local kinetic mapping are provided in the ESI (ESI Figure S-14 to S-16). The three methods used to determine rate constant data produce results that showe similar trends, i.e., values for the rate constants determined by either bulk EIS method or local methods decrease after anodic ageing and partially recover after cathodic reactivation. As shown in Table 1, compared to the EIS results, the results for the approach curve method differ more significantly than those for the kinetic mapping method. A Welch's t-test was performed on the data to determine at what level the mean values for the two local methods are statistically different than that obtained for the bulk EIS method, and the results are summarized in ESI Table S-12. Results indicate that the values determined for the average rate constants using EIS and kinetic mapping are statistically equivalent at > 95% confidence interval ($p > 0.05$), and those determined by EIS analysis and the approach curve method are not ($p < 0.05$) (Table S-12). These results indicate that the local kinetic mapping method produces results that are statistically equivalent to the bulk EIS kinetic method and the

approach curve method does not. These results are attributed to the fact that the kinetic mapping method contains a larger population of interrogated spots (N = 32000) than the approach curve method (N = 20), and thus the heterogeneity of the sample is averaged over more observations. The consistency between local SECM and bulk EIS methods indicates the accuracy of the SECM method to provide spatially resolved data that is useful for accurate surface characterization.

3.3 Effect of Magnéli Phase on Hydroxyl Radical Production. The $OH^{\bullet}$ production is critical to operation of EAOPs, due to its ability to react with organic compounds at diffusion limited rates.[47,64] In this study, changes among the Magnéli phases are not observed, however, electrode preparation often results in the presence of various Magnéli phases and it is also possible that phase change can occur after extended polarizations.[24] In order to examine the influence of the Ti_nO_{2n-1} composition on $OH^{\bullet}$ production, five samples with different Magnéli phase compositions were synthesized. The XRD spectra for these samples are shown in Figure 4A, and the average values for n that are determined using Equation 6 are provided in Figure 4B. The rate constant for terephthalic acid is calculated in a dead-end flow-through reactor (Figure 1), and $[OH^{\bullet}]_s$ are determined using Equation 7.

The $[OH^{\bullet}]_s$ values are inversely proportional to the resistivity of the Ti_nO_{2n-1} electrode (Figures 4A and 4B). Sample 1 possesses a composition of pure Ti_4O_7 and exhibited the highest $[OH^{\bullet}]_s$ ($2.6\times10^{-11} \pm 1\times10^{-12}$ mol m^{-2}). The other samples contain a mixture of higher oxidation state Magnéli phases, and their ability to produce $OH^{\bullet}$ decreases with increasing oxidation state (or n value) (Figure 4B).

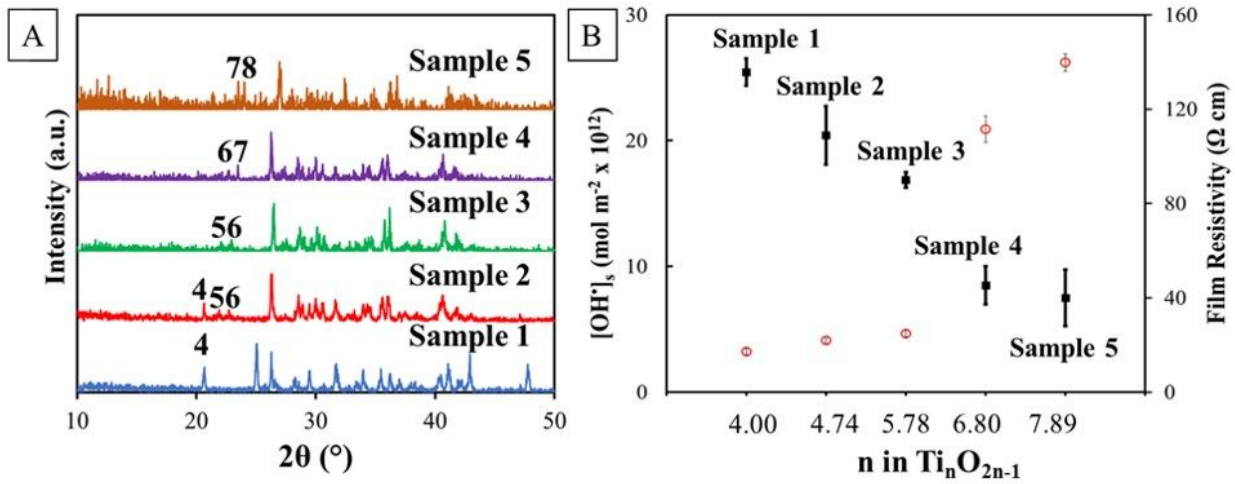

Figure 4 (A) XRD patterns of different Magnéli phase samples (number above the characteristic peak indicates n in Ti_nO_{2n-1}), and (B) steady state surface $OH^{\bullet}$ concentration (■) and film resistivity (○) of different samples in a dead-end flow-through setup at room temperature. Solution: 0.1 mM terephthalic acid in 1 M KH_2PO_4 (pH 5.8). The solution resistance corrected anodic potentials on Sample 1 to 5 are 3.3, 3.3, 3.4, 3.4 and 3.4 V, respectively. Permeate flux on Sample 1 to 5 (LMH): 780, 840, 900, 720, 1080. Pressure drop across electrode: 1.03 bar. Error bars represent 95% confidence interval.

The kinetic variations of $OH^{\bullet}$ formation on the Ti_nO_{2n-1} electrodes of different resistivities can be explained by an electron tunneling mechanism in the space-charge layer.[46] At a constant applied anodic potential on the n-type Ti_nO_{2n-1} semiconductor electrode, band bending will introduce a space-charge layer near the electrode surface, where electrons are depleted.[65] The width of the space charge layer (d_{sc}) is inversely proportional to N_D. Therefore, a larger N_D will produce a thinner d_{sc}, and in turn a higher electron tunneling probability. For example, at an applied potential of 2.8 V vs Ag/AgCl, which is suitable for $OH^{\bullet}$ production on Ti_nO_{2n-1},[18,66] the values for d_{sc} increases from 0.17 nm at sample 1 (n = 4.00) to 9.1 nm at sample 5 (n = 7.89), as shown in Table S-13. It is reported that electron tunneling can only take place when d_{sc} is less than 1-2 nm,[67] which indicates Ti_nO_{2n-1} with a higher oxidation state is less electrochemically active due to a larger d_{sc}. It should be noted that the values for d_{sc}, when n is greater than 5.78, are beyond the electron tunneling width, but reactivity for $OH^{\bullet}$ formation is still observed, which could be

attributed to the heterogeneity of the energy band structure, N_D, local conductivity, electric field induced band bending, and electron hopping.[65] Meanwhile, it is observed that the band gap of Ti_nO_{2n-1} increases with respect to n, which leads to extra resistance in transferring electrons from the valence band to the conduction band.[11,68–75] Furthermore $OH^{\bullet}$ formation may also be attributed to different free energies of adsorption for $OH^{\bullet}$ ($\Delta G_{OH\bullet}$) at the different Ti_nO_{2n-1} phases. It has been postulated that the criterion for $OH^{\bullet}$ formation is that $\Delta G_{OH\bullet}$ is greater than the free energy of a solvated $OH^{\bullet}$.[76] Therefore, more investigation is needed to determine the exact mechanism responsible for $OH^{\bullet}$ production at the Ti_nO_{2n-1} electrodes.

Although the effect that substrate polarization has on $OH^{\bullet}$ production was not carried out in this study experimentally, results from the analysis above suggest that $OH^{\bullet}$ production would be diminished after the anodic ageing, and recovered after the cathodic reactivation, since, for example in the H_2SO_4 electrolyte, the values for ρ_f increase from 18.67 ± 0.02 Ω cm at the pristine state to 132.70 ± 0.004 Ω cm after anodic ageing, and decrease to 33.94 ± 0.001 Ω cm after 30-min cathodic reactivation. Therefore, operating at an optimal oxidation state and frequent cathodic reactivation are necessary to maintain the high reactivity of Ti_nO_{2n-1} for $OH^{\bullet}$ production.

3.4 Mechanism of Anodic Ageing and Cathodic Reactivation in Different Electrolytes. In both the $HClO_4$ and HCl electrolytes, measured values for N_D, film conductivity, and charge transfer kinetics decrease after anodic ageing and increase after cathodic reactivation. Phase changes are not found, however peak shifts in the XRD data are observed on the electrodes polarized in these electrolytes, and therefore, it suggests that the changes in electronic properties are likely associated with the doping level through intercalation in the Ti_nO_{2n-1} samples. From the structural point of view, Magnéli phases can be interpreted as an ordered combination of rutile TiO_2 and corundum Ti_2O_3 layers. It has been reported that small ions, such as protons, can insert

into the *c*-direction channels in the TiO_2 structure, and act as shallow electron donors,[62,63] which suggests that proton intercalation can also occur in the rutile TiO_2 layer of the Magnéli phase. Although direct evidence has not been reported regarding proton intercalation into Ti_2O_3, researchers have investigated Li^+ intercalation into Ti_2O_3 during the charge and discharge of lithium ion batteries, which implies that proton, a smaller ion compared to Li^+, could also be intercalated in the shear planes. It is also reported that Magnéli phases have *d*-spacings that are larger than anatase or rutile TiO_2, indicating its likeness for proton intercalation.[77,78] Furthermore, electrochemical polarization allows intercalation to a much higher proton concentration.[79] In the pristine samples, these point sites originate from the dissociative adsorption of H_2 on the pristine TiO_2 surface during the synthesis process, followed by a charge transfer reaction between adsorbed H atoms and Ti^{4+} sites to form Ti^{3+} sites (Reaction 8).

$$H_2 + 2Ti^{[4+]}O_2 \rightarrow 2Ti^{[3+]}OOH \qquad (8)$$

The formation of these point Ti^{3+} sites, which are distinctly different from Ti^{3+} sites located in the shear plane, result in increasing the electronic conductivity.[80] During the anodic ageing, point Ti^{3+} sites near the Ti_nO_{2n-1} surface were oxidized to Ti^{4+}, and therefore the excess charge was removed by H^+ discharge from the electrode, as shown in Reaction 9.[7]

$$Ti^{[3+]}O_2\text{-}H^+ \leftrightarrow Ti^{[4+]}O_2 + H^+ + e^- \qquad (9)$$

During the cathodic reactivation, the donor sites can be reincorporated into the sample by H^+ intercalation (reverse of Reaction 9), and thus the electronic conductivity and charge transfer kinetics were recovered.[46,61,80] It is reported that the H^+ intercalation can be readily achieved in an acidic media under a negative polarization, since the high proton concentration of the electrolyte facilitates the intercalation process.[80] Experimental evidence supports the H^+ reversible

intercalation process, as CV scans show two anodic peaks at 0.2 V and 1.0 V vs Ag/AgCl, which are likely related to the release of intercalated protons at different locations in the crystal lattice (Reaction 9) (Figure 5 and ESI Figure S-20).[81]

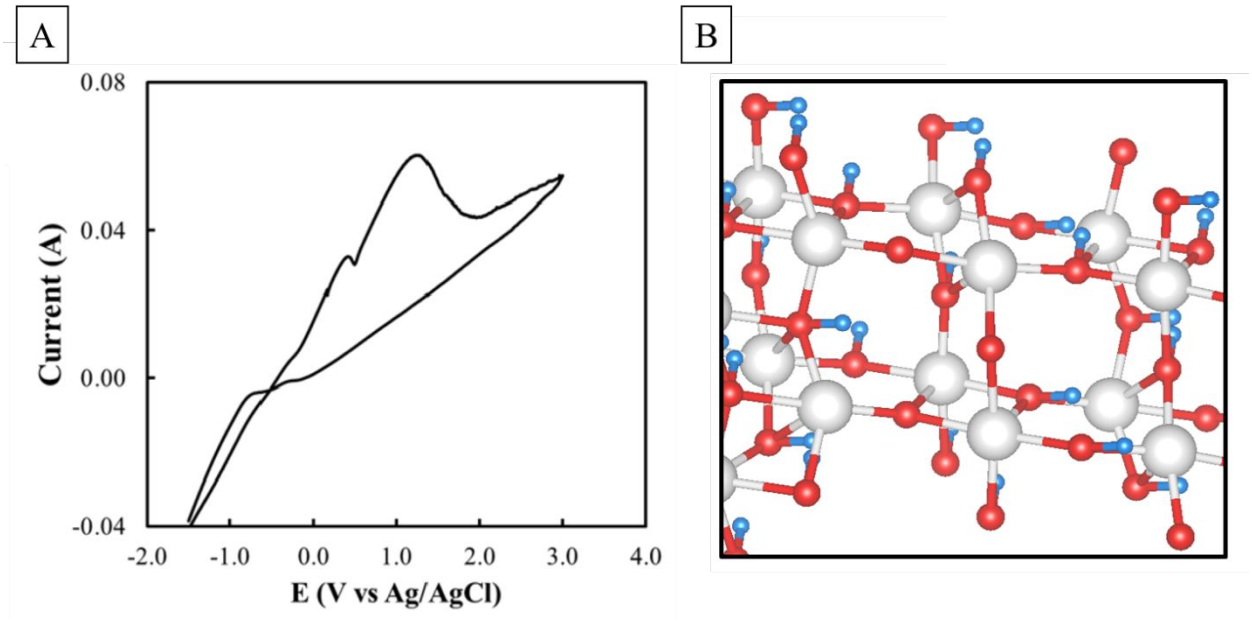

Figure 5. (A) CV scan on Ti_nO_{2n-1} in 1 M H_2SO_4 supporting electrolyte showing the intercalation process, scan rate: 0.1 V s^{-1}, and (B) schematic showing the likely sites for H^+ intercalation in Ti_4O_7 (1-20). The image is looking into the c channels of Ti_4O_7 (1-20). Atom key: Red = oxygen; grey = titanium; and blue = hydrogen.

The more substantial passivation and lower recovery after cathodic reactivation for the H_2SO_4 electrolyte relative to other electrolytes, supports the hypothesis that additional passivation mechanisms are affecting the performance of Ti_nO_{2n-1} in the presence of H_2SO_4. Contrary to the results in the $HClO_4$ and HCl electrolytes, the Ti_nO_{2n-1} sample polarized in the H_2SO_4 electrolyte shows a crystal structure change. The XRD results in Figure 2A contain peaks that suggest the formation of a $TiOSO_4$ film. It is generally accepted that oxygen vacancies arrange themselves upon sufficient annealing, and Magnéli phases are associated with a crystal structure rearrangement that leads to a local Ti_2O_3 corundum structure at the shear planes and contains very

few point oxygen vacancy sites.[82,83] A value for E_a = 64 kJ mol^{-1} is estimated from the TGA data for converting Ti_4O_7 to Ti_6O_{11} (ESI Section S-21). This value is relatively low, but Magnéli phase change is not expected during anodic ageing at ambient temperatures, as the oxidation of Ti_4O_7 only occurs at temperatures > 350 ^oC (ESI Figure S-18), where defects are more easily formed and solid-state diffusion rates are greatly increased.[84] Therefore, the observed loss of electrochemical reactivity of Ti_nO_{2n-1} in the presence of H_2SO_4 may also be attributed to the complexation of SO_4^{2-} with Ti atoms at the electrode surface in addition to the discharge of H^+.

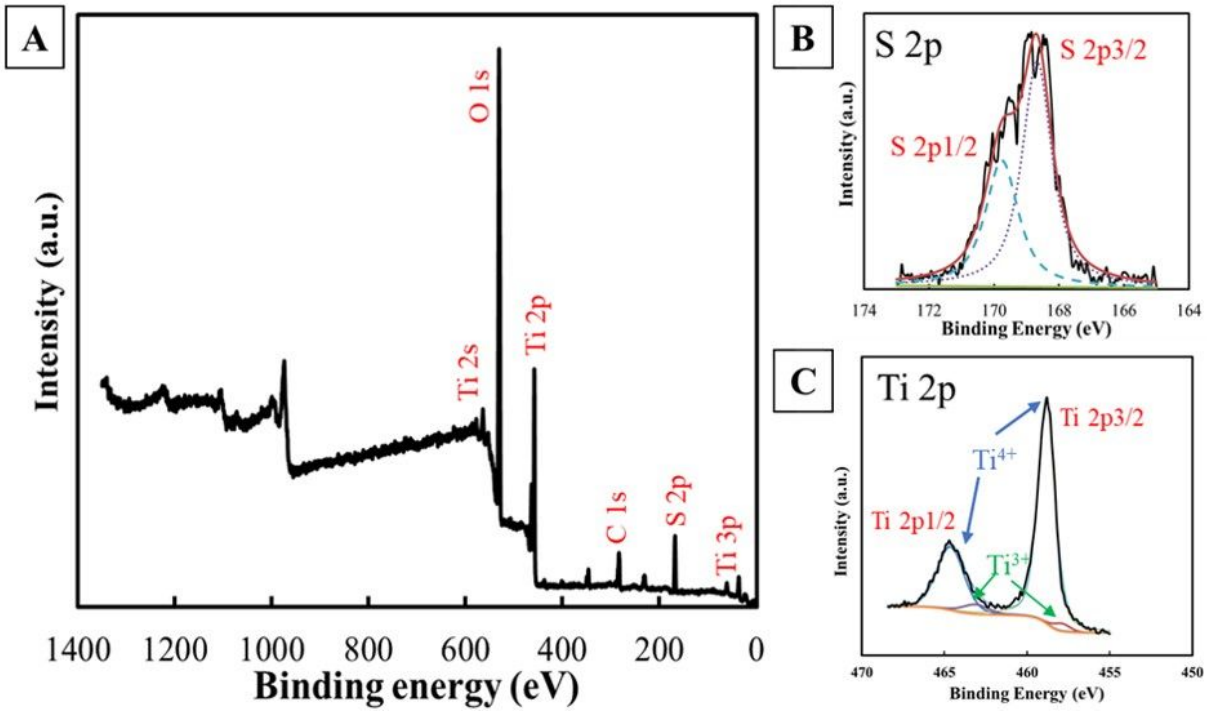

Figure 6. XPS spectra of Ti_nO_{2n-1} electrode after 30 mins of anodic ageing in 1 M H_2SO_4 electrolyte at 20 mA cm^{-2}. (A) Full spectrum, (B) S 2p doublet regions, and (C) Ti 2p doublet regions.

Analysis of the samples by XPS supports the hypothesis that the complexation of SO_4^{2-} or $SO_4^{\bullet-}$ at the electrode surface occurred. XPS analysis detects the presence of SO_4^{2-} at 9.5% atomic percentage on the electrode surface after the anodic ageing (20 mA cm^{-2}) in 1 M H_2SO_4 electrolyte

for 30 min (Figure 6A), while 3.5% atomic percent is observed on the control sample, which is left at OCP in 1 M H_2SO_4 for 30 min. XPS results are discussed in more detail in the ESI Section S-23. The surface sulfate present on the control sample may be attributed to residual sulfate after the cleaning process, which either does not induce a change in the XRD spectra or is below the XRD detection limit (ESI Figure S-6). The above observations suggest that the loss of electronic conductivity and electrochemical reactivity of the Ti_nO_{2n-1} sample after anodic ageing in the H_2SO_4 electrolyte is partially attributed to the formation of a surface passivation layer with a major constituent of $TiOSO_4$.

To provide additional support for the proposed SO_4^{2-} complexation mechanism, DFT simulations were performed to determine ΔU_a values for the adsorption of SO_4^{2-} to the Ti_4O_7 (1-20) surface according to the following reaction:

$$\mathrm{SO}_{4(\mathrm{aq})}^{2-} + \mathrm{Ti}[\ ] \leftrightarrow \mathrm{Ti}[\mathrm{SO}_4]_{\mathrm{ad}} + 2\mathrm{e}^- \qquad (10)$$

where Ti[ ] represents an empty adsorption site and $\mathrm{Ti}[\mathrm{SO}_4]_{\mathrm{ad}}$ represents the adsorbed sulfate species. The Ti_4O_7 (1-20) surface was chosen because it was a strong peak detected by XRD (see Figure 2). The potential dependent adsorption energy for sulfate ($\Delta U_a(E)$) was calculated according to the following equation.

$$\Delta U_{\mathrm{a}}(E) = U_{\mathrm{Ti}[\mathrm{SO}_4]_{\mathrm{ad}}} - U_{\mathrm{Ti}[\ ]} - U_{\mathrm{SO}_{4(\mathrm{aq})}^{2-}} - 2eE \qquad (11)$$

where e represents the electron charge. The DFT optimized structures are shown in the ESI (Figures S-21 to S-22). To determine the anodic potential for which the SO_4^{2-} oxidation reaction was activationless, the E_a vs. potential profile for the oxidation of SO_4^{2-} was calculated for Reaction 12.

$$SO_4^{2-} \rightarrow SO_4^{\bullet-} + e^- \quad (12)$$

Results are shown in the ESI (Figure S-23), and indicate that the reaction is activationless at potentials > 1.85 V vs Ag/AgCl. Therefore, the ΔU_a value for SO_4^{2-} adsorption at the Ti_4O_7 (1-20) surface was calculated at 1.85 vs Ag/AgCl and yielded a value of ΔU_a = -8.4 eV. These results indicate a very strong adsorption energy for SO_4^{2-} at the Ti_4O_7 surface, and supported the surface passivation mechanism discussed above.

4. Conclusions

Maintaining a high electronic conductivity and electrochemical reactivity is key to the success of Ti_nO_{2n-1} electrodes in electrochemical advanced oxidation processes, visible light photocatalysis, and energy conversion devices in order to achieve the best performance. This study found that the mechanism for the loss of electronic conductivity and electrochemical reactivity during anodic polarization depends on the type of electrolyte. In both the ClO_4^- and Cl^- electrolytes decreased conductivity and electrochemical reactivity are attributed to the decrease in the donor concentration, specifically that from H^+ doping. Meanwhile, in the SO_4^{2-} electrolyte a combined effect of a decrease in the donor concentration and formation of $TiOSO_4$ surface species is responsible for the loss of electronic conductivity and electrochemical reactivity. However, the electronic conductivity and electrochemical reactivity can be recovered through cathodic reactivation, and thus a regular cathodic reactivation is necessary to intercalate H^+ and remove the $TiOSO_4$ passivating layer.

From the results of this study, the surface deactivation is expected when Ti_nO_{2n-1} is used as an anode, which is attributed to the formation of a passivation film or loss of charge carriers (proton and Ti^{3+} donor center). In many studies, Ti_nO_{2n-1} has been used as a cathode material, such as in

lithium-sulfur,[4] lead-acid,[24,27] and zinc-air[25,26] batteries. Therefore, surface deactivation of Ti_nO_{2n-1} would primarily occur during the charging process, and a surface deactivated Ti_nO_{2n-1} would act as a barrier to electron flow. Such a process would cause capacity loss and poor cycling stability.[35] Due to its reversible nature, during the discharge process surface deactivation on Ti_nO_{2n-1} may be gradually reduced by either reintroducing charge carriers or removing the passivation film, however the high resistance associated with surface deactivation will cause an ohmic drop immediately after a load is placed on the cell.[85] Hence, in many applications the ohmic drop may cause the electrode potential to be below the minimum operating potential, and thus a pre-condition of the cell may be necessary.

Conflicts of Interest

There are no conflicts to declare.

Acknowledgement

Funding for this work was provided by the National Science Foundation (CBET-1159764 and CBET-1453081 (CAREER)). We thank Pralay Gayen for the XPS measurement, Dr. Berry and his research group for performing two-point probe measurement, and Songwei Che for the XPS peak fitting and discussion. Portions of this work were carried out in the Nano Core Facility and Electron Microscopy Service *via* the Research Resources Center at the University of Illinois at Chicago.

References

1 G. Wang, Y. Yang, D. Han and Y. Li, *Nano Today*, 2017, **13**, 23–39.

2 G. Wang, H. Wang, Y. Ling, Y. Tang, X. Yang, R. C. Fitzmorris, C. Wang, J. Z. Zhang and Y. Li, *Nano Lett.*, 2011, **11**, 3026–3033.

3 X. Pan, M.-Q. Yang, X. Fu, N. Zhang and Y.-J. Xu, *Nanoscale*, 2013, **5**, 3601–14.

4 X. Tao, J. Wang, Z. Ying, Q. Cai, G. Zheng, Y. Gan, H. Huang, Y. Xia, C. Liang, W. Zhang and Y. Cui, *Nano Lett.*, 2014, **14**, 5288–5294.

5 H. J. Yun, D. M. Lee, S. Yu, J. Yoon, H. J. Park and J. Yi, *J. Mol. Catal. A Chem.*, 2013, **378**, 221–226.

6 L. Liborio, G. Mallia and N. Harrison, *Phys. Rev. B - Condens. Matter Mater. Phys.*, 2009, **79**, 1–9.

7 G. Chen, C. C. Waraksa, D. D. Macdonald, T. E. Mallouk, C. C. Waraksa, H. Cho, D. D. Macdonald and T. E. Mallouka, *J. Electrochem. Soc.*, 2003, **150**, E423.

8 M. V. Ganduglia-Pirovano, A. Hofmann and J. Sauer, *Surf. Sci. Rep.*, 2007, **62**, 219–270.

9 G. Lu, a Linsebigler and J. T. Yates, *J. Phys. Chem.*, 1994, **98**, 11733–11738.

10 A. F. Arif, R. Balgis, T. Ogi, F. Iskandar, A. Kinoshita, K. Nakamura and K. Okuyama, *Sci. Rep.*, 2017, **7**, 3646.

11 M. Abbate, R. Potze, G. A. Sawatzky, C. Schlenker, H. J. Lin, L. H. Tjeng, C. T. Chen, D. Teehan and T. S. Turner, *Phys. Rev. B*, 1995, **51**, 10150–10153.

12 S. Harada, K. Tanaka and H. Inui, *J. Appl. Phys.*, 2010, **108**, 083703.

13 D. S. Jeong, R. Thomas, R. S. Katiyar, J. F. Scott, H. Kohlstedt, A. Petraru and C. S. Hwang, *Reports Prog. Phys.*, 2012, **75**, 076502.

14 K. Szot, M. Rogala, W. Speier, Z. Klusek, A. Besmehn and R. Waser, *Nanotechnology*, 2011, **22**, 254001.

15 J. Kwon, A. A. Sharma, J. A. Bain, Y. N. Picard and M. Skowronski, *Adv. Funct. Mater.*, 2015, **25**, 2876–2883.

16 M. C. Santos, Y. A. Elabd, Y. Jing, B. P. Chaplin and L. Fang, *AIChE J.*, 2016, **62**, 508–524.

17 L. Guo, Y. Jing and B. P. Chaplin, *Environ. Sci. Technol.*, 2016, **50**, 1428–1436.

18 A. M. Zaky and B. P. Chaplin, *Environ. Sci. Technol.*, 2013, **47**, 6554–63.

19 D. Bejan, E. Guinea and N. J. Bunce, *Electrochim. Acta*, 2012, **69**, 275–281.

20 D. Bejan, J. D. Malcolm, L. Morrison and N. J. Bunce, *Electrochim. Acta*, 2009, **54**, 5548–5556.

21 O. Scialdone, A. Galia and G. Filardo, *Electrochim. Acta*, 2008, **53**, 7220–7225.

22 M. Toyoda, T. Yano, B. Tryba and S. Mozia, *Appl. Catal. B Environ.*, 2009, **88**, 160–164.

23 R. Zhu, Y. Liu, J. Ye and X. Zhang, *J. Mater. Sci. Mater. Electron.*, 2013, **24**, 4853–4856.

24 W. Kao, P. Patel and S. L. Haberichter, *J. Electrochem. Soc.*, 1997, **144**, 1907.

25 X. Li, A. L. Zhu, W. Qu, H. Wang, R. Hui, L. Zhang and J. Zhang, *Electrochim. Acta*, 2010, **55**, 5891–5898.

26 C. Tang, Z. Debi, S. Fang and L. Yang, *J. Electrochem. Soc.*, 2012, **159**, 1983–1988.

27 K. Ellis, A. Hill, J. Hill, A. Loyns and T. Partington, *J. Power Sources*, 2004, **136**, 366–371.

28 A. C. M. Padilha, H. Raebiger, A. R. Rocha and G. M. Dalpian, *Sci. Rep.*, 2016, **6**, 28871.

29 C. Yao, F. Li, X. Li and D. Xia, *J. Mater. Chem.*, 2012, **22**, 16560.

30 D. Rajkumar and K. Palanivelu, *J. Hazard. Mater.*, 2004, **113**, 123–129.

31 T. Ioroi, Z. Siroma, N. Fujiwara, S. Yamazaki and K. Yasuda, *Electrochem. commun.*, 2005, **7**, 183–188.

32 K. Senevirathne, R. Hui, S. Campbell, S. Ye and J. Zhang, *Electrochim. Acta*, 2012, **59**, 538–547.

33 S. El-Sherif, D. Bejan and N. J. Bunce, *Can. J. Chem.*, 2010, **88**, 928–936.

34 G. Oriji, Y. Katayama and T. Miura, *Electrochim. Acta*, 2004, **49**, 3091–3095.

35 Z. Liu and P. P. Mukherjee, *ACS Appl. Mater. Interfaces*, 2017, **9**, 5263–5271.

36 B. P. Chaplin, *Environ. Sci. Process. Impacts*, 2014, **1**, 1182–1203.

37 J. Pouilleau, D. Devilliers, H. Groult and P. M. Arcus, *J. Mate Rials Sci.*, 1997, **32**, 5645–5651.

38 A. K. Neufeld and A. P. O'Mullane, *J. Solid State Electrochem.*, 2006, **10**, 808–816.

39 N. Wilson, S. Clewes, M. Newton, P. Unwin and J. Macpherson, *J. Phys. Chem. B*, 2006, **110**, 5639.

40 K. B. Holt, A. J. Bard, Y. Show and G. M. Swain, *J. Phys. Chem. B*, 2004, **108**, 15117–15127.

41 M. C. Granger, M. Witek, J. Xu, J. Wang, M. Hupert, A. Hanks, M. D. Koppang, J. E. Butler, G. Lucazeau, M. Mermoux, J. W. Strojek and G. M. Swain, *Anal. Chem.*, 2000, **72**, 3793–3804.

42 S. Amemiya, A. J. Bard, F.-R. F. Fan, M. V. Mirkin and P. R. Unwin, *Annu. Rev. Anal. Chem.*, 2008, **1**, 95–131.

43 C. Lefrou and R. Cornut, *ChemPhysChem*, 2010, **11**, 547–556.

44 M. V Mirkin, F.-R. F. Fan and A. J. Bard, *J. Electroanal. Chem.*, 1992, **328**, 47–62.

45 Y. Jing and B. P. Chaplin, *Environ. Sci. Technol.*, 2017, **51**, 2355–2365.

46 Y. Yang and M. R. Hoffmann, *Environ. Sci. Technol.*, 2016, **50**, 11888–11894.

47 G. V. Buxton, C. L. Greenstock, W. P. Helman and A. B. Ross, *J. Phys. Chem. Ref. Data*, 1988, **17**, 513.

48 J. B. Foresman and Æ. Frische, *Exploring chemistry with electronic structure methods: a guide to using Gaussian*, Gaussian Inc., Pittsburgh, PA, 2nd edn., 1996.

49 M. Frisch, G. Trucks, H. Schlegel, G. Scuseria, M. Robb, J. Cheeseman, G. Scalmani, V. Barone, B. Mennucci and G. Petersson, 2009.

50 A. V Marenich, C. J. Cramer and D. G. Truhlar, *J. Phys. Chem. B*, 2009, **113**, 6378–6396.

51 G. Kresse and J. Furthmüller, *Comput. Mater. Sci.*, 1996, **6**, 15–50.

52 G. Kresse and D. Joubert, *Phys. Rev. B*, 1999, **59**, 1758–1775.

53 G. Kresse and J. Furthmüller, *Phys. Rev. B*, 1996, **54**, 11169–11186.

54 P. E. Blöchl, *Phys. Rev. B*, 1994, **50**, 17953–17979.

55 K. Momma and F. Izumi, *J. Appl. Crystallogr.*, 2011, **44**, 1272–1276.

56 M. Fujioka, C. Wu, N. Kubo, G. Zhao, A. Inoishi, S. Okada, S. Demura, H. Sakata, M. Ishimaru, H. Kaiju and J. Nishii, *J. Am. Chem. Soc.*, 2017, **139**, 17987–17993.

57 A. R. Armstrong, G. Armstrong, J. Canales, R. García and P. G. Bruce, *Adv. Mater.*, 2005, **17**, 862–865.

58 D. Aurbach and Y. Ein-Eli, *J. Electrochem. Soc.*, 1995, **142**, 1746–1752.

59 S. Nayak and B. P. Chaplin, *Electrochim. Acta*, 2018, **263**, 299–310.

60 A. W. Bott, *Curr. Sep.*, 1998, **17**, 87–92.

61 H. Wu, D. Li, X. Zhu, C. Yang, D. Liu, X. Chen, Y. Song and L. Lu, *Electrochim. Acta*, 2014, **116**, 129–136.

62 J. Sasaki, N. L. Peterson and K. Hoshino, *J. Phys. Chem. Solids*, 1985, **46**, 1267–1283.

63 C. G. Van De Walle, *Phys. Rev. Lett.*, 2000, **85**, 1012–1015.

64 W. Pryor, *Annu. Rev. Physiol.*, 1986, **48**, 657–667.

65 Z. Zhang and J. T. Yates, *Chem. Rev.*, 2012, **112**, 5520–5551.

66 A. M. Zaky and B. P. Chaplin, *Environ. Sci. Technol.*, 2014, **48**, 5857–67.

67 H. Lüth, *Solid Surfaces, Interfaces and Thin Films*, Springer International Publishing, Cham, Sixth., 2015.

68 M. Uchida, J. Fujioka, Y. Onose and Y. Tokura, *Phys. Rev. Lett.*, 2008, **101**, 1–4.

69 Y. Guo, S. J. Clark and J. Robertson, *J. Phys. Condens. Matter*, 2012, **24**, 325504.

70 V. Singh and J. J. Pulikkotil, *J. Alloys Compd.*, 2016, **658**, 430–434.

71 R. Liu, J. X. Shang and F. H. Wang, *Comput. Mater. Sci.*, 2014, **81**, 158–162.

72 D. Kaplan, C. Schlenker and J. J. Since, *Philos. Mag.*, 1977, **36**, 1275–1279.

73 I. Leonov, A. N. Yaresko, V. N. Antonov, U. Schwingenschlögl, V. Eyert and V. I. Anisimov, *J. Phys. Condens. Matter*, 2006, **18**, 10955–10964.

74 P. Lv, H. Sun, Y. Mu, S. Su, Y. Chen, H. Yao, D. Ding, Y. Ma, W. Fu and H. Yang, *Electrochim. Acta*, 2014, **146**, 186–193.

75 I. Slipukhina and M. Ležaić, *Phys. Rev. B*, 2014, **90**, 155133.

76 S. Siahrostami, G.-L. Li, V. Viswanathan and J. K. Nørskov, *J. Phys. Chem. Lett.*, 2017, **8**, 1157–1160.

77 H. J. Song, J. C. Kim, C. W. Lee, S. Park, M. A. Dar, S. H. Hong and D. W. Kim, *Electrochim. Acta*, 2015, **170**, 25–32.

78 A. R. Park, D. Y. Son, J. S. Kim, J. Y. Lee, N. G. Park, J. Park, J. K. Lee and P. J. Yoo, *ACS Appl. Mater. Interfaces*, 2015, **7**, 18483–18490.

79 M. V. Koudriachova, S. W. De Leeuw and N. M. Harrison, *Phys. Rev. B - Condens. Matter Mater. Phys.*, 2004, **70**, 1–5.

80 F. Fabregat-santiago, E. M. Barea, J. Bisquert, G. K. Mor, K. Shankar and C. a Grimes, *J. Am. Chem. Soc.*, 2008, **130**, 11312–11316.

81 J. Przyłuski and K. Kolbrecka, *J. Appl. Electrochem.*, 1993, **23**, 1063–1068.

82 L. Liborio and N. Harrison, *Phys. Rev. B - Condens. Matter Mater. Phys.*, 2008, **77**, 1–10.

83 H. Nörenberg and G. A. D. Briggs, *Surf. Sci.*, 1998, **402–404**, 738–741.

84 H. Liu, H. . Ma, X. . Li, W. . Li, M. Wu and X. . Bao, *Chemosphere*, 2003, **50**, 39–46.

85 C. Tran, J. Kafle, X. Q. Yang and D. Qu, *Carbon N. Y.*, 2011, **49**, 1266–1271.

Surface deactivation and reactivation processes on the Magnéli phase electrode surface in H_2SO_4 electrolyte